ARTICLE

Surface-enhanced charge-density-wave instability in underdoped $Bi_2Sr_{2-x}La_xCuO_{6+\delta}$

J.A. Rosen[1,*], R. Comin[1,*], G. Levy[1,2], D. Fournier[1], Z.-H. Zhu[1], B. Ludbrook[1], C.N. Veenstra[1], A. Nicolaou[1,2], D. Wong[1], P. Dosanjh[1], Y. Yoshida[3], H. Eisaki[3], G.R. Blake[4], F. White[5], T.T.M. Palstra[4], R. Sutarto[6], F. He[6], A. Fraño Pereira[7,8], Y. Lu[7], B. Keimer[7], G. Sawatzky[1,2], L. Petaccia[9] & A. Damascelli[1,2]

Neutron and X-ray scattering experiments have provided mounting evidence for spin and charge ordering phenomena in underdoped cuprates. These range from early work on stripe correlations in Nd-LSCO to the latest discovery of charge-density-waves in $YBa_2Cu_3O_{6+x}$. Both phenomena are characterized by a pronounced dependence on doping, temperature and an externally applied magnetic field. Here, we show that these electron-lattice instabilities exhibit also a previously unrecognized bulk-surface dichotomy. Surface-sensitive electronic and structural probes uncover a temperature-dependent evolution of the CuO_2 plane band dispersion and apparent Fermi pockets in underdoped $Bi_2Sr_{2-x}La_xCuO_{6+\delta}$ (Bi2201), which is directly associated with an hitherto-undetected strong temperature dependence of the incommensurate superstructure periodicity below 130 K. In stark contrast, the structural modulation revealed by bulk-sensitive probes is temperature-independent. These findings point to a surface-enhanced incipient charge-density-wave instability, driven by Fermi surface nesting. This discovery is of critical importance in the interpretation of single-particle spectroscopy data, and establishes the surface of cuprates and other complex oxides as a rich playground for the study of electronically soft phases.

[1] Department of Physics and Astronomy, University of British Columbia, Vancouver, British Columbia, Canada V6T 1Z1. [2] Quantum Matter Institute, University of British Columbia, Vancouver, British Columbia, Canada V6T 1Z4. [3] National Institute of Advanced Industrial Science and Technology (AIST), Tsukuba 305-8568, Japan. [4] Materials Science Centre, University of Groningen, Nijenborgh 4, 9747 AG Groningen, The Netherlands. [5] Agilent Technologies UK Ltd., 10 Mead Road, Oxford Industrial Park, Yarnton, Oxfordshire OX5 1QU, UK. [6] Canadian Light Source, University of Saskatchewan, Saskatoon, Saskatchewan, Canada S7N 0X4. [7] Max Planck Institute for Solid State Research, Heisenbergstrasse 1, D-70569 Stuttgart, Germany. [8] Helmholtz-Zentrum Berlin für Materialien und Energie, Wilhelm-Conrad-Röntgen-Campus BESSY II, Albert-Einstein-Strasse 15, D-12489 Berlin, Germany. [9] Elettra Sincrotrone Trieste, Strada Statale 14 Km 163.5, 34149 Trieste, Italy. * These authors contributed equally to this work. Correspondence and requests for materials should be addressed to A.D. (email: damascelli@physics.ubc.ca).

The underdoped cuprates, with their pseudogap phenomenology[1–3] and marked departure from Fermi liquid behavior[4], have led to proposals of a wide variety of possible phases ranging from conventional charge and magnetic order to nematic and unconventional density-wave instabilities[5–27]. Despite the extensive theoretical and experimental effort, the generic phase behavior of the underdoped cuprates is still a matter of heated debate, primarily because of the lack of an order parameter that could be universally associated with the underdoped regime of the high-T_c cuprates (HTSCs). For instance, early on, evidence was obtained for long-range spin and charge order in the form of uniaxial stripes[6]. This phenomenology has been detected in compounds belonging to the La_{2-x-y}(Sr,Ba)$_x$(Nd,Eu)$_y$CuO$_4$ family[6,28–30], namely Eu-LSCO, Nd-LSCO, LBCO, and recently also pristine LSCO (where stripe order appears as a near-surface effect[31]), and it is historically associated with the family-specific reduction of superconducting T_c near 12% doping, the so-called '1/8-anomaly'.

More recently, high-field quantum oscillations[17], Hall resistance[32] and thermoelectric transport[33] results on underdoped YBa$_2$Cu$_3$O$_{6+x}$ (YBCO) were interpreted as a signature of a magnetic field-induced reconstruction of the normal-state Fermi surface, suggesting that stripe order and/or a charge-density-wave (CDW) phase might be more general features of HTSCs' underdoped regime. Interest in this direction has been burgeoning with the latest NMR[34], resonant X-ray scattering (REXS) and X-ray diffraction (XRD) results[35–37], providing direct evidence for a long-range incommensurate CDW in YBCO around 10–12% hole doping, which further shows a suppression for $T < T_c$ and an enhancement with increasing magnetic field. Although this phenomenon bears some differences with respect to charge stripes, a common intriguing aspect is that they both are electronically driven forms of ordering and appear to compete with superconductivity.

If a CDW phase in underdoped cuprates is universal, it should be observable in compounds with similar doping levels regardless of their structural details. In addition, it is of fundamental importance to connect structural observations (XRD and REXS) to those of electronic probes, such as angle-resolved photoemission (ARPES) and scanning tunneling (STM) spectroscopy. However, for YBCO this might be prevented altogether by the polar instability and self-doping of the (001) surface; in fact, ARPES studies have not yet directly detected a folding of the electronic band structure[4,38] carrying the signature of a symmetry-broken CDW state as otherwise seen in either quantum oscillation[17] or XRD experiments[35–37]. To broaden the search and attempt this connection, the most interesting family is the one of Bi-cuprates which, owing to their extreme two-dimensionality and natural cleavage planes, have been extensively studied by single-particle spectroscopies[39,40]. ARPES and STM have provided rich insight into the electronic properties of the CuO$_2$ plane, including signatures of broken symmetries[10,13,14,16,24,27,26,41] and hints of a 'pseudogap phase-transition'[26], although the identification of a bona fide order parameter has remained elusive. More specifically, in regards to a potentially underlying CDW instability, pristine Bi-cuprates have been shown to exhibit multiple superstructures, and while some of these modulations originate from the structural mismatch between BiO and CuO$_2$ lattice planes and hence are non-electronic in origin[39,42–45], others have been recognized by STM to evolve strongly with doping and magnetic field[11,12,20,25]; however, their relationship to the 'structural' superstructures and the Fermi surface has remained unclear. Our experimental results will provide new and surprising insight in this direction.

Here, we study the structural and electronic properties of Bi$_2$Sr$_{2-x}$La$_x$CuO$_{6+\delta}$ (Bi2201), whose crystal structure exhibits a stacking of well-spaced, single CuO$_2$ layers in the unit cell and a highly ordered superstructure[45], by means of surface-sensitive
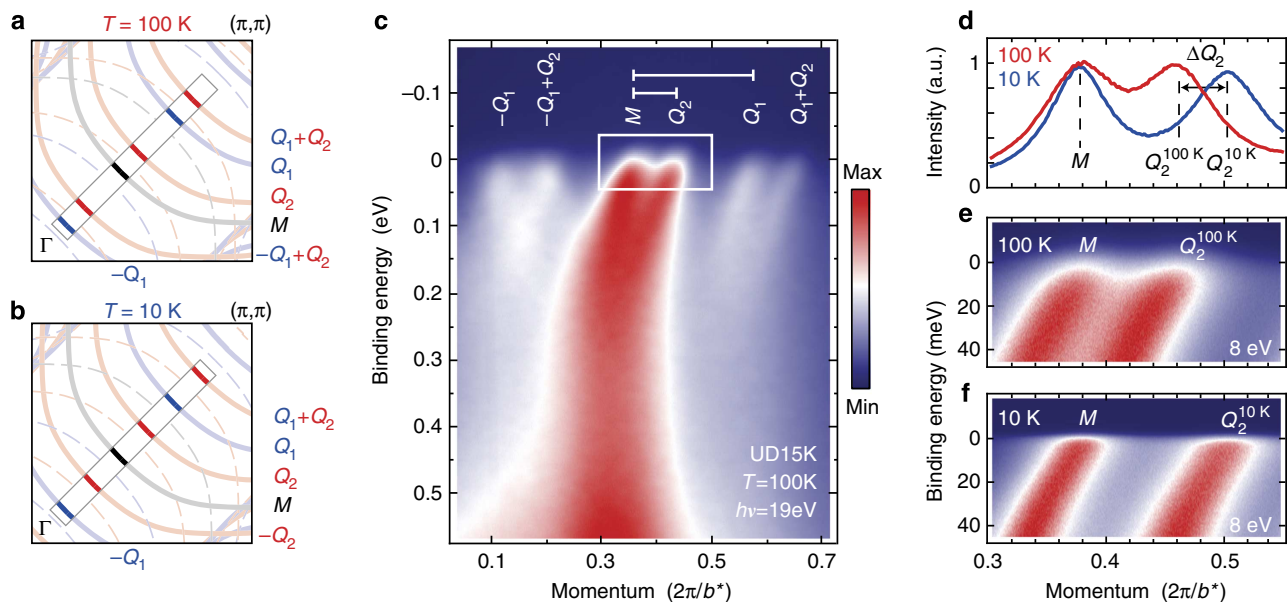
Figure 1 | Temperature dependence of the nodal electronic structure of UD15K Bi2201. (a,b) Sketch of one quadrant of the tetragonal Brillouin zone for $T = 100$ and 10 K, respectively; indicated are the expected Fermi surfaces belonging to the main band (M) and its replicas due to different $\mathbf{Q_1}$ and $\mathbf{Q_2}$ superstructure vector combinations (solid lines), as well as all the corresponding backfolded features due to the orthorhombicity of the crystal (dashed lines, so-called 'shadow-bands'). The nodal strip in (**a,b**) highlights the region measured by ARPES with various photon energies and temperatures in (**c,e,f**), and the six bands detected for this experimental geometry and polarization (the photon polarization is set in the plane of detection to suppress all but the main band and its replicas). MDCs at E_F for 10 and 100 K are directly compared in (**d**). Also note that in (**c–f**), as throughout the paper, momentum axes are expressed in units of $2\pi/a^*$ and $2\pi/b^*$, where $a^* \cong b^* \cong \sqrt{2} \times 3.86$ Å refer to the orthorhombic unit cell of Bi2201 (3.86 Å is the in-plane Cu-O-Cu distance).
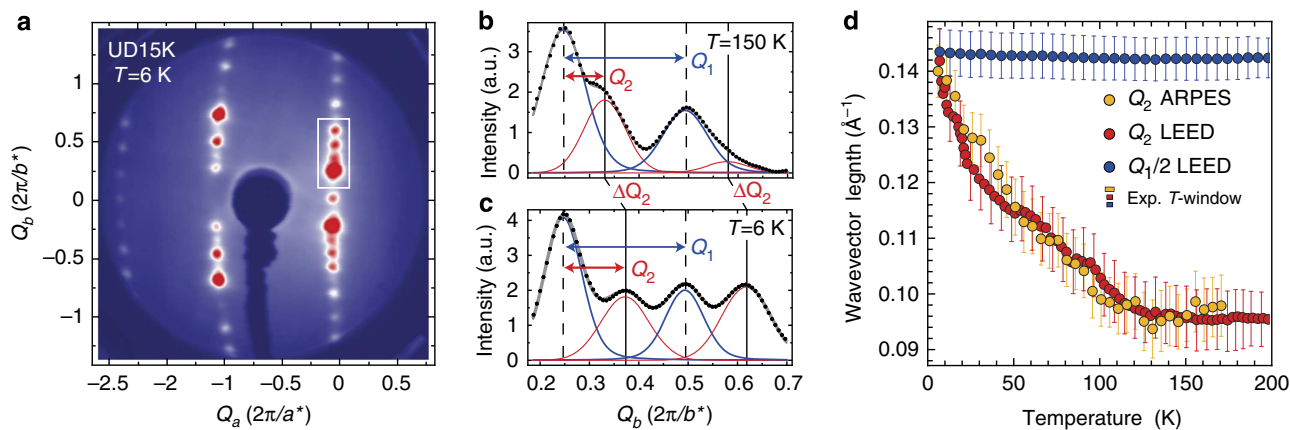
Figure 2 | Temperature dependence of the superstructure modulations of UD15K Bi2201. (**a**) Typical LEED pattern measured at $T = 6$ K. The rectangular box in (**a**) highlights the region shown in detail for $T = 150$ and 6 K in (**b**) and (**c**), respectively. In (**b,c**) symbols represent the data from a vertical cut along the center of the box in (**a**), while blue and red curves are a Voigt fit of the $\mathbf{Q_1}$ and $\mathbf{Q_2}$ superstructure peaks. (**d**) Magnitude of the $\mathbf{Q_1}$ and $\mathbf{Q_2}$ superstructure vectors in $Å^{-1}$ versus temperature, as inferred from LEED and ARPES-MDC analysis at 21 eV photon energy (and in agreement with ARPES from 7 to 41 eV, see Fig. 1). The yellow and red/blue boxes indicate the temperature integration window of each data point, for ARPES (5 K) and LEED (3 K), respectively, and the error bars show the goodness of fit for the Voigt profiles determined from a χ^2 test. Note that, for the almost temperature-independent $\mathbf{Q_1}$, half of the actual value is plotted for a more direct comparison with $\mathbf{Q_2}$ and only the LEED data are shown (the ARPES data are equivalent and thus omitted).

photoemission spectroscopy (ARPES) and low-energy electron diffraction (LEED) probes, as well as bulk-sensitive resonant (REXS) and non-resonant XRD. We focus on the temperature dependence of the electronic structure from under ($p \simeq 0.12$, $T_c = 15$ K, UD15K) to nearly optimal doping ($p \simeq 0.16$, $T_c = 30$ K, OP30K). We discover a temperature-dependent evolution of the CuO$_2$ plane band dispersion and apparent Fermi surface pockets, which is directly associated with the evolution of the incommensurate superstructure. Surprisingly, this effect is limited to the surface (ARPES–LEED), with no corresponding temperature evolution in the bulk (XRD–REXS). The quasilinear, continuous variation of the surface modulation wavelength $2\pi/Q_2$ from $\sim$66 to 43 Å, below a characteristic $T_{Q_2} \simeq 130$ K, provides evidence for a surface-enhanced CDW instability, driven by the interplay of nodal and antinodal Fermi surface nesting.

Results

**Orthorhombic and modulated structure of the Bi-cuprates.** An important aspect to consider for the study of Bi-cuprates is that these materials are not structurally tetragonal, but instead orthorhombic, with two inequivalent Cu atoms per CuO$_2$ plane[39,42–45]. This leads to a 45° degree rotated and $\sqrt{2} \times \sqrt{2} \times 1$ larger unit cell, as compared with the tetragonal one, with lattice parameters $a^* \cong b^* \cong \sqrt{2} \times 3.86$ Å, where 3.86 Å is the planar Cu-O-Cu distance ($c \cong 24.9$ Å; for both structures). Note that throughout the paper we refer to the orthorhombic unit cell, with momentum axes expressed using the reciprocal lattice units (r.l.u.) $2\pi/a^*$, $2\pi/b^*$ and $2\pi/c^*$. The orthorhombicity and consequent band backfolding have been shown to be responsible for the observation of the so-called 'shadow bands'[44], a replica of the hole-like CuO$_2$ Fermi surface centered at the Γ point, thus settling a longstanding debate on their possible antiferromagnetic origin[46]. In addition, the presence of incommensurate superstructure modulations, arising from a slight lattice mismatch between the BiO layers and the CuO$_2$ perovskite blocks[47], further adds to the complexity of the Fermi surface. As for single-layer Bi2201 specifically, while a single $\mathbf{Q_1}$ superstructure vector is known to give rise to additional folded replicas along the orthorhombic b^* axis at optimal doping (OP)[39],

two distinct structural modulations with $\mathbf{Q_1}$ and $\mathbf{Q_2}$ wavevectors arise with underdoping (UD). If these complications are not fully taken into account in analyzing ARPES data, the resulting highly complex Fermi surface appears to be composed of a small set of closed pockets[45].

Probing the surface with ARPES and LEED. We begin with the discussion of the UD15K Bi2201 ARPES data from along the nodal direction presented in Fig. 1. As demonstrated in previous work[45], and here sketched in Fig. 1a,b for a simpler identification of the various bands, the high crystallinity of these samples allows resolving the Fermi surface of Bi-cuprates to an unprecedented level of detail: the main (M) CuO$_2$-plane band (black solid line), its $\mathbf{Q_1}$ and $\mathbf{Q_2}$ superstructure replicas stemming from the BiO-layer-induced incommensurate superstructure (red and blue solid lines), and all the corresponding backfolded bands due to the orthorhombicity of the crystal (dashed lines). Furthermore, as shown in Fig.1c for UD15K at $T = 100$ K, and emphasized in the highlighted nodal strip in Fig. 1a, by taking advantage of the polarization-dependent selection rules[45], one can selectively suppress the redundant backfolded bands to highlight more cleanly the behavior of main (M) and $\mathbf{Q_1}$–$\mathbf{Q_2}$ bands. The ability to simultaneously detect all superstructure replicas allows us to uncover—in the temperature dependence—a new and unprecedented aspect of the data: while the position of the main CuO$_2$ band is completely temperature-independent, between 100 and 10 K there is a significant shift in momentum of only (and all) the $\mathbf{Q_2}$-related bands [see Fig. 1e,f, and Fig. 1d for the direct comparison between 10–100 K momentum distribution curves (MDCs) at E_F]. This is summarized in the 10 K Fermi surface sketch of Fig. 1b, which illustrates that a critical consequence of this effect is a seeming volume change of all ostensible Fermi surface pockets defined by the various backfolded bands, despite the fact that the actual number of carriers is not changing at all.

The ARPES results are complemented by a detailed analysis of the superstructure diffraction vectors from LEED. On UD15K at 6 K, rather than individual Bragg peaks (Fig. 2a), the experiment gives lines of $\mathbf{Q_1}$ and $\mathbf{Q_2}$ fractional spots along the orthorhombic
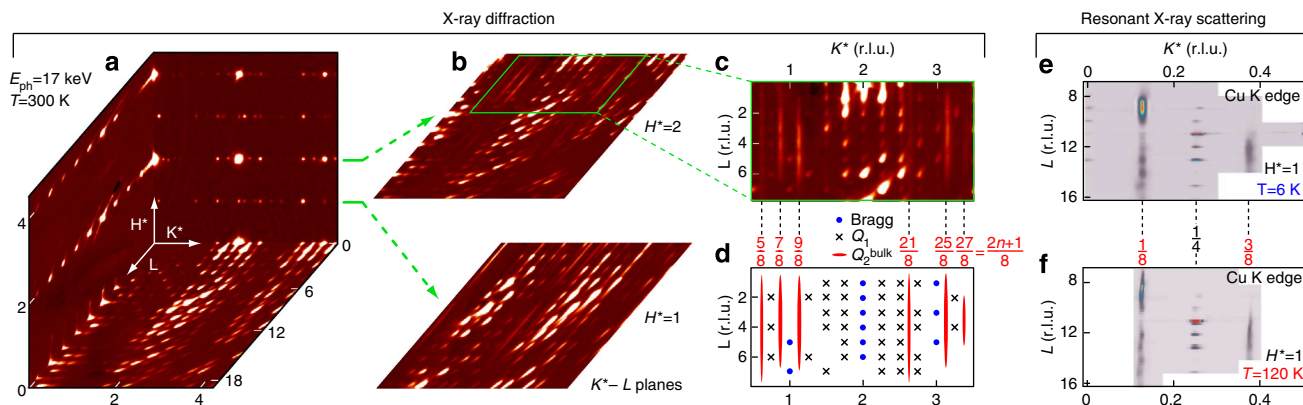
Figure 3 | X-ray measurements of the superstructure modulations in UD15K Bi2201. (**a**) Three-dimensional view of the basal planar sections of XRD maps at $E_{ph} \sim 17\,keV$ (only positive axes are shown). (**b**) $H^\star = 1, 2$ slices, showing the appearance of period-8 diffraction rods, while no similar features are found for $H^\star = 0$ [see bottom plane in panel (**a**)], thus explaining the lack of period-8 features in soft X-ray REXS. (**c**) Enlarged view of corresponding region of interest in (**b**) for the $H^\star = 2$ slice. (**d**) Schematic cartoon explaining the multiple features that are visible in (**c**): blue circles correspond to Bragg peaks for integer $K^\star$ and L orders; black crosses are the 1/4-order $\mathbf{Q}_1$ peaks; red ellipses are the 1/8-order $\mathbf{Q}_2$ peaks. (**e**) REXS map acquired at the Cu-K edge ($E_{ph} \sim 8.9\,keV$) at 6 K, representing a $\mathbf{K}^\star$–$\mathbf{L}$ plane at $H^\star = 1$. (**f**) Same as (**e**), but acquired at 120 K.

$b^\star$ axis. From the fit of the LEED data (Fig. 2c), we obtain for the magnitude of the superstructure wavevectors, the values $Q_1^{6K} = 0.285 \pm 0.015\,\text{Å}^{-1}$ and $Q_2^{6K} = 0.142 \pm 0.015\,\text{Å}^{-1}$, corresponding to $\sim 1/4$ and $1/8$ in r.l.u., respectively. Also LEED, on this highly resolved superstructure, reveals a remarkable temperature dependence (Fig. 2b,c). Consistent between LEED and ARPES–MDC analysis (Fig. 2d), while Q_1 is virtually temperature-independent from 5 to 300 K, Q_2 increases with respect to its high-temperature value $Q_2^{300K} = 0.095 \pm 0.015\,\text{Å}^{-1}$ ($\sim 1/12$ in r.l.u.) below a $T_{Q_2} \simeq 130\,K$. The evolution of Q_2—as seen by both electronic and structural probes—implies an inter-unit-cell structural and/or electronic modulation, with a wavelength $2\pi/Q_2$ evolving from 66 to 44 Å (that is, from 12 to 8 $\times b^\star$) upon cooling from 130 down to 5 K.

Bulk sensitivity with XRD and REXS. The surface sensitivity of ARPES and LEED calls for an investigation of the same phenomenology by means of light-scattering techniques, which are known to probe materials deeper in the bulk. In the following discussion, we will refer to reciprocal space coordinates as $\mathbf{H}^\star$, $\mathbf{K}^\star$ and $\mathbf{L}$ (representing the reciprocal axes of, respectively, $\mathbf{a}^\star$, $\mathbf{b}^\star$ and $\mathbf{c}$), and reciprocal lattice units will be used. At all photon energies, it is possible to clearly identify the supermodulation associated with $\mathbf{Q}_1$. In particular, REXS maps taken on UD15K Bi2201 at the Cu, La, and O soft X-ray edges all exhibit a clear enhancement at this wavevector (see Supplementary Note 1 for details). This confirms that the corresponding modulation is present throughout the unit cell, and therefore also in the CuO$_2$ plane, explaining the strong folded replicas observed in ARPES. However, modulations with longer periods are not detected. These can be probed by XRD maps measured at 17 keV photon energy, thus revealing a much larger portion of reciprocal space, as shown in Fig. 3a–c for $T = 300\,K$. The $\mathbf{H}^\star$–$\mathbf{K}^\star$section in Fig. 3a, which can be compared with the LEED map in Fig. 2a, also features a multitude of superstructure satellite peaks along $\mathbf{K}^\star$(the Bragg peaks being the most intense ones). Figure 3b displays the $\mathbf{K}^\star$–$\mathbf{L}$ sections for $H^\star = 1, 2$, which reveal the presence of new features exhibiting a peculiar elongation along $\mathbf{L}$ and period-8 modulation along $\mathbf{K}^\star$ with positions given by $K^\star = (2n+1)/8$. The latter are therefore incompatible with the near period-4 modulation associated with $\mathbf{Q}_1$ or any of its harmonics (also note that no similar

features are found for $H^\star = 0$, thus explaining the lack of period-8 rods in soft X-ray REXS, which due to kinematic constraints can only probe a reduced portion of reciprocal space). Different orders of this period-8 modulation can be seen when zooming in to the $H^\star = 2$ slice in Fig. 3c, with their assignment given more schematically in Fig. 3d. These are located at positions $\mathbf{Q}_2^{ij} = n\mathbf{G} \pm i\mathbf{Q}_1 \pm j\mathbf{Q}_2$, where $\mathbf{G}$ is a reciprocal lattice vector, $\mathbf{Q}_1 = 1/4\hat{\mathbf{u}}_{K^\star}$, and $\mathbf{Q}_2 = 1/8\hat{\mathbf{u}}_{K^\star}$ (corresponding to the ARPES and LEED low-temperature $\mathbf{Q}_2^{6K}$ value). Notably, the same features can be seen in resonant scattering at Cu and Bi deeper edges (that is, in the hard X-ray regime). Figures 3e,f show corresponding $\mathbf{K}^\star$–$\mathbf{L}$ sections ($H^\star = 1$), taken at the Cu-K edge at low (6 K) and high (120 K) temperature, respectively. Additional data for the Bi-L_3 edge and the temperature-dependent XRD maps are shown in Supplementary Note 1.

The intensity of the $\mathbf{Q}_2^{ij}$ rods is ~ 1 order of magnitude smaller than the most intense $\mathbf{Q}_1$ peak, within the same $\mathbf{K}^\star$–$\mathbf{L}$ sections. Considering the large probing depth of hard X-rays, this intensity ratio is too large to identify these as crystal truncation rods, or ascribe them to surface modulations. These period-8 spots therefore originate from an additional supermodulation that must be present in the bulk of the material, and characterized by poor c axis coherence, as the elongated structure suggests. On the other hand, these features exhibit long-range order in the $\mathbf{a}^\star$–$\mathbf{b}^\star$ plane, as evidenced by their well-defined shape in $\mathbf{H}^\star$–$\mathbf{K}^\star$ sections, with correlation lengths $\xi > 100 \times b^\star$.

To summarize the findings from XRD and REXS on UD15K, no significant temperature dependence is observed between 300 and 6 K in all scans, neither in the peak positions nor in the relative intensities. Altogether, these results suggest a scenario involving the presence of an additional bulk supermodulation with a well-defined periodicity along $\mathbf{b}^\star$ (~ 8 lattice periods), stable over a broad range of temperatures, and characterized by large correlation lengths within the (001) planes, but poor coherence perpendicular to them.

Discussion

The combination of surface (ARPES and LEED)- and bulk (XRD and REXS)-sensitive probes has enabled us to establish that $\mathbf{Q}_1$ and $\mathbf{Q}_2$ superstructure modulations are present both in the bulk and at the surface of underdoped Bi2201, close to 1/8 doping
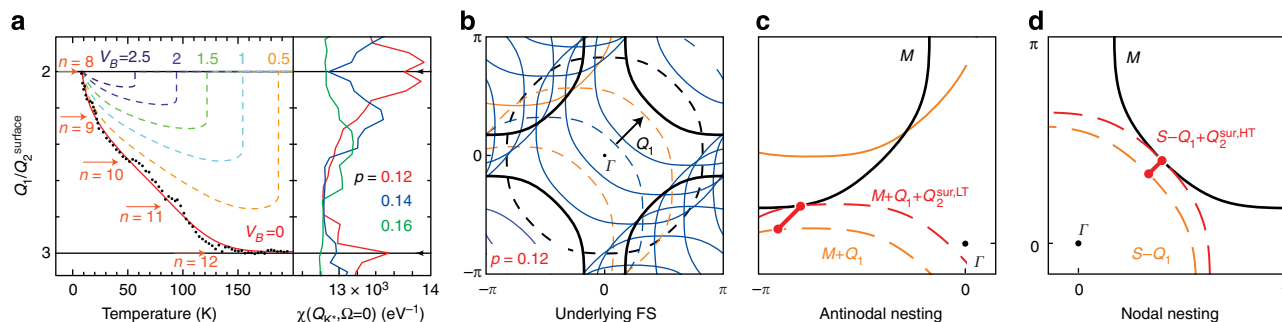
Figure 4 | Q_2 mean-field theory and nesting effects in the electronic susceptibility. (**a**, main panel) Temperature evolution of the Q_1/Q_2^{surf} wave vector magnitude ratio (black dots), as inferred from the LEED data in Fig. 2, compared with the evolution of the mean-field predicted wavevector that minimizes the free energy (Supplementary Note 2); red arrows mark those wavevectors at which the modulation associated with $\mathbf{Q}_2$ becomes commensurate with the underlying orthorhombic lattice $Q_2 = (2\pi/b^*)/n$, for various values of n. The colored curves illustrate the effect of increasing V_B, showing how the bulk structure can pin the CDW and suppress the temperature dependence of $\mathbf{Q}_2$. (**a**, side panel) Calculated electronic susceptibility $\chi(\mathbf{Q})$, cut along the $\mathbf{K}^*$ direction in reciprocal space, for $p = 0.12$ (red), 0.14 (blue) and 0.16 (green). (**b**) Cartoon of the Fermi surface modeling used in the calculation of $\chi(\mathbf{Q})$; orange traces mark the Fermi surfaces involved in the nesting mechanism ($M + Q_1$ and $S - Q_1$). (**c,d**) Schematics of the antinodal and nodal nesting instabilities, which connect the main (M, black trace) band with $M + Q_1$ and $S - Q_1$ (orange traces), respectively. The resulting nesting vectors $\mathbf{Q}_2^{surf,LT}$ and $\mathbf{Q}_2^{surf,HT}$ are represented by the thick red connectors, while the corresponding $\mathbf{Q}_2$-derived Fermi surfaces are shown in dashed red.

(UD15K). In addition, we have uncovered an unprecedented bulk-surface dichotomy in the temperature dependence of the superstructure modulations and corresponding electronic structure. While no dependence is observed for the $\mathbf{Q}_1$ and $\mathbf{Q}_2$ superstructure in the bulk and also for $\mathbf{Q}_1$ at the surface, we detected a pronounced temperature evolution associated with the surface $\mathbf{Q}_2^{surf}$. As for the doping dependence of this phenomenon, while the $\mathbf{Q}_1$ modulation survives all the way to optimal doping ($Q_1 \simeq 0.280$ and 0.273 Å^{-1} for UD23K and OP30K, respectively), the $\mathbf{Q}_2$ modulation is substantially weakened and temperature-independent for UD23K ($p = 0.14$, $Q_2 \simeq 0.135$ Å^{-1}), and can no longer be detected in either LEED or ARPES on OP30K ($p > 0.16$). This is discussed in the Supplementary Note 1 based on the doping and temperature-dependent LEED, ARPES and X-ray data.

The dependence of the Q_1/Q_2^{surf} ratio versus temperature for UD15K is summarized in Fig. 4a and allows some important phenomenological observations: (i) the temperature dependence of $\mathbf{Q}_2^{surf}$ below T_{Q_2} shows commensurability with the static $\mathbf{Q}_1$ modulation, as evidenced by the Q_1/Q_2^{surf} ratio varying from 3 to 2 over a range of 130 K. (ii) The evolution of Q_1/Q_2^{surf} exhibits a possible transient lock-in behavior when the wavelength of the $\mathbf{Q}_2^{surf}$ modulation is commensurate with the orthorhombic lattice: $2\pi/Q_2^{surf} = n \times b^*$, with n ranging from 12 to 8, as marked by red arrows in Fig. 4a (see also Supplementary Note 2 for a more extended discussion). A similar albeit more pronounced behavior has been observed for charge-stripe order in La$_2$NiO$_{4+\delta}$ from neutron scattering[48]. (iii) In analogy to what was reported for manganites[49], the continuous evolution of incommensurate wave vectors over a wide temperature range hints at competing instabilities, which can lead to a soft electronic phase. (iv) Finally, the fact that at low-temperature (LT) also $\mathbf{Q}_2^{surf,LT} \simeq \mathbf{Q}_2^{bulk}$ indicates a direct connection between the bulk and surface modulations.

We have succeeded in reproducing the details of the observed CDW instability and its temperature evolution using a two-fold analysis (detailed in Supplementary Notes 2 and 3) involving: (i) the evaluation of the electronic susceptibility [through the zero-temperature, zero-frequency Lindhard function $\chi(\mathbf{Q}, \Omega = 0)$]; and (ii) a mean-field Ginzburg–Landau model based on an *ad-hoc* phenomenological free-energy functional $F[\rho]$, typical of

that applied to CDW systems. The electronic susceptibility $\chi(\mathbf{Q}, \Omega = 0)$ has been calculated for various doping levels starting from an electronic structure comprised of main, shadow and $\mathbf{Q}_1$-folded bands (see Fig. 4b) and is shown for $p = 0.12$, 0.14 and 0.16 in the right-hand side panel of Fig. 4a. Two peaks occur in the susceptibility along the $\mathbf{K}^*$ direction in reciprocal space at $Q_{K^*} = 0.095$ and 0.140 Å^{-1} for $p = 0.12$, closely matching the $\mathbf{Q}_2$ supermodulation vectors for UD15K. This allows associating $\mathbf{Q}_2^{surf,HT} \simeq \mathbf{Q}_1/3$ and $\mathbf{Q}_2^{surf,LT} \simeq \mathbf{Q}_1/2$ with nodal and anti-nodal Fermi surface nesting, that is, $Q_2^{surf,HT} = Q_{K^*}^N = 0.095$ and $Q_2^{surf,LT} = Q_{K^*}^{AN} = 0.140$ Å^{-1} (these denominations designate the region in k-space where bands overlap maximally, as pictorially shown in Fig. 4c,d). These nesting instabilities are very sensitive to the hole doping, especially for the steeper nodal dispersion; for $p = 0.14$ and 0.16, the nodal peak abruptly vanishes, while the antinodal is split—and therefore ceases to be commensurate to $\mathbf{Q}_1$—and gradually reduced and broadened towards optimal doping, yielding a progressively less pronounced instability. These findings qualitatively explain the experimentally observed progressive weakening of the features associated with $\mathbf{Q}_2$ as hole doping is increased (discussed in Supplementary Note 1). Ultimately, this establishes the specific high- and low-temperature values observed for the surface CDW modulation on UD15K, $\mathbf{Q}_2^{surf,HT}$ and $\mathbf{Q}_2^{surf,LT}$, to be associated with competing Fermi surface nesting instabilities of the $\mathbf{Q}_1$-modulated orthorhombic crystal structure. Most importantly, this identifies the temperature-dependent $\mathbf{Q}_2$ surface CDW as a phenomenon limited to the underdoped regime, near 1/8 doping, consistent with our experimental observations.

As for the origin of the observed temperature dependence, the evolution of Q_1/Q_2^{surf} (ratio of wavevector magnitude) is well captured by a phenomenological Ginzburg–Landau description based on the minimization of the surface free-energy functional $F[\rho]$, and is thus consistent with an incipient CDW instability at the surface. This is shown by the comparison of LEED and theoretical results (red trace) for the evolution of Q_1/Q_2^{surf} in UD15K, shown in Fig. 4a. Commensurability to the susceptibility peaks ($Q_1/Q_2^{surf} = 2$ and 3) underpins the low- and high-temperature limits, while the free energy $F[\rho]$, in absence of a bulk potential, provides a modeling of the surface, and accounts for the temperature dependence of the $\mathbf{Q}_2$ wavevector. In

Ginzburg–Landau mean-field theory, this can be understood as a consequence of the temperature-dependent harmonic content of a non-sinusoidal CDW (see Supplementary Note 2 and Supplementary Discussion for more on this point), which here coincides with the Q_1/Q_2 commensurability effects.

In our Ginzburg–Landau description, we can also include the effect of the bulk potential V_B associated with the 'static' $\mathbf{Q}_2^{bulk}$ modulation as determined by XRD ($V_B = |V_{Q_2}|$, with V_{Q_2} as defined in Supplementary Note 2). As shown by the simulated colored traces in Fig. 4a, incorporating this potential progressively causes the CDW to lock in to the bulk structural modulation wavevector $\mathbf{Q}_2^{bulk} = \mathbf{Q}_1/2$ at $V_B \sim 3.0$, thus suppressing the temperature dependence. The two regimes $V_B = 0$ and $V_B > 3$ represent the temperature-dependent-surface and temperature-independent-bulk limiting cases, providing agreement with the results of ARPES–LEED on the surface and XRD–REXS for the bulk. Intermediate values of V_B describe the subsurface region, which shows a CDW with reduced dependence on temperature, and instability towards first-order lock-in transitions to the $\mathbf{Q}_2^{bulk}$ wavevector (see dashed traces in Fig. 4a).

In conclusion, the temperature-dependent evolution of the CuO$_2$ plane band dispersion and $\mathbf{Q}_2$ superstructure on the highly ordered Bi2201 surface can be understood to arise from the competition between nodal and antinodal Fermi surface nesting instabilities, which give rise to a dynamic, continuously evolving wavevector. This also indicates that such a remarkable electron-lattice coupling is directly related to the ordinary, static $\mathbf{Q}_1$ superstructure—as a necessary precursor to Fermi surface nesting at the low- and high-temperature $\mathbf{Q}_2^{surf}$—and giving rise to commensurability effects. As the nodal nesting-response is very sensitive to the hole doping, this also explains why the surface temperature dependence disappears towards optimal doping. This establishes the importance of surface-enhanced CDW nesting instabilities in underdoped Bi-cuprates, and reveals a so-far undetected bulk-surface dichotomy. The latter is responsible for many important implications, such as the temperature-dependent volume change of all apparent Fermi surface pockets in ARPES, and could have a hidden role in other temperature-dependent studies.

Methods

Sample preparation. For this study, we used two underdoped ($x = 0.8$, $p \simeq 0.12$, UD15K and $x = 0.6$, $p \simeq 0.14$, UD23K) and one optimally doped ($x = 0.5$, $p \simeq 0.16$, OP30K) Bi$_2$Sr$_{2-x}$La$_x$CuO$_{6+\delta}$ single crystals (p is the hole doping per planar copper away from half-filling). The superconducting $T_c = 15$, 23 and 30 K, respectively, were determined by in-plane resistivity and magnetic susceptibility measurements. For UD15K, we found T$^* \simeq 190$ K, based on the onset of the deviation of the resistivity-versus-temperature curve from the purely linear behavior observed at high temperatures.

ARPES and LEED experiments. ARPES measurements were performed at UBC with 21.2 eV photon energy (HeI), and at the Elettra synchrotron BaDElPh beamline with photon energy ranging from 7 to 41 eV. In both cases, the photons were linearly polarized and the polarization direction—horizontal (p) or vertical (s)—could be varied with respect to the electron emission plane. Both ARPES spectrometers are equipped with a SPECS Phoibos 150 hemispherical analyzer; energy and angular resolution were set to 6–10 meV and 0.1°. The samples were aligned by conventional Laue diffraction prior to the experiments and then mounted with the in-plane Cu-O bonds either parallel or at 45° with respect to the electron emission plane. LEED measurements were performed at UBC with a SPECS ErLEED 100; momentum resolution was set to 0.01 Å^{-1} by using a low electron energy of 37 eV, at which value the signal intensity reaches a maximum. During the LEED measurements, the samples were oriented with the orthorhombic b^* axis, vertical in reference to the camera, and rotated by 7° in the horizontal plane to detect more spots. For both LEED and ARPES, the samples were cleaved in situ at pressures better than 5×10^{-11} torr. The detailed temperature-dependent experiments were performed on the UBC ARPES spectrometer, which is equipped with a five-axis helium-flow cryogenic manipulator operating between 2.7 and 300 K. The ARPES (LEED) data were acquired at 0.5 frame per s (30 frame per s), while the sample was cooled at a continuous rate of 0.1 K min^{-1} (1 K min^{-1}). The ARPES (LEED) data were averaged over 1,500 (5,400) images, resulting in

ARPES spectra (LEED curves) with a temperature precision of 5 K (3 K). The higher temperature accuracy achieved in LEED stems from its ten-fold signal-to-noise ratio as compared with ARPES.

Light scattering experiments. Resonant elastic soft X-ray measurements were taken using a four-circle diffractometer at the REIXS beamline at the Canadian Light Source, working at the O-K ($E_{ph} \sim 530$ eV), La-$M_{4,5}$ ($E_{ph} \sim 836$ eV) and Cu-$L_{2,3}$ ($E_{ph} \sim 930$ eV) absorption edges. Hard X-ray scans were performed using a psi-8 diffractometer (8-circle) at the Mag-S beamline at BESSY, working at the Cu-K ($E_{ph} \sim 8.9$ keV) and Bi-L_3 ($E_{ph} \sim 13.2$ keV) deep edges. Both soft and hard X-ray scattering measurements were performed in the temperature range 15–300 K. XRD reciprocal space maps were acquired using an Agilent Technologies SuperNova A diffractometer. The data were collected at 300 K and 100 K using Mo-K_a and Cu-K_a radiation, respectively. The excitation energies used for these experiments correspond in turn to approximate attenuation lengths (α) of ~ 150 nm (Cu-$L_{2,3}$), 6 µm (Cu-K) and 12 µm (Mo-K_a). In all cases, samples were pre-oriented using Laue diffraction and mounted **b*** and **c** axes in the scattering plane. In order to expose an atomically flat (001) surface, in- and ex- situ cleaving procedures were adopted for soft and hard X-ray measurements, respectively.

References

1. Timusk, T. & Statt, B. The pseudogap in high-temperature superconductors: an experimental survey. *Rep. Prog. Phys* **62**, 61–122 (1999).
2. Norman, M. R., Pines, D. & Kallin, C. The pseudogap: friend or foe of high-T_c? *Adv. Phys* **54**, 715–733 (2005).
3. Hüfner, S., Hossain, M. A., Damascelli, A. & Sawatzky, G. A. Two gaps make a high-temperature superconductor? *Rep. Prog. Phys* **71**, 062501 (2008).
4. Fournier, D. *et al.* Loss of nodal quasiparticle integrity in underdoped YBa$_2$Cu$_3$O$_{6+x}$. *Nat. Phys* **6**, 905–911 (2010).
5. Zaanen, J. & Gunnarsson, O. Charged magnetic domain lines and the magnetism of high-T_c oxides. *Phys. Rev. B* **40**, 7391–7394 (1989).
6. Tranquada, J. M., Sternlieb, B. J., Axe, J. D., Nakamura, Y. & Uchida, S Evidence for stripe correlations of spins and holes in copper oxide superconductors. *Nature* **375**, 561–563 (1995).
7. Varma, C. M. Non-fermi-liquid states and pairing instability of a general model of copper oxide metals. *Phys. Rev. B* **55**, 14554 (1997).
8. Kivelson, S. A., Fradkin, E. & Emery, V. J. Electronic liquid-crystal phases of a doped mott insulator. *Nature* **393**, 550–553 (1998).
9. Chakravarty, S., Laughlin, R. B., Morr, D. K. & Nayak, C. Hidden order in the cuprates. *Phys. Rev. B* **63**, 094503 (2001).
10. Kaminski, A. *et al.* Spontaneous breaking of time-reversal symmetry in the pseudogap state of a high-T_c superconductor. *Nature* **416**, 610–613 (2002).
11. Hoffman, J. E. *et al.* A four unit cell periodic pattern of quasi-particle states surrounding vortex cores in Bi$_2$Sr$_2$CaCu$_2$O$_{8+\delta}$. *Science* **295**, 466–469 (2002).
12. Howald, C., Eisaki, H., Kaneko, N. & Kapitulnik, A. Coexistence of periodic modulation of quasiparticle states and superconductivity in Bi$_2$Sr$_2$CaCu$_2$O$_{8+\delta}$. *Proc. Natl Acad. Sci. USA* **100**, 9705–9709 (2003).
13. Vershinin, M. *et al.* Local ordering in the pseudogap state of the high-t_c superconductor Bi$_2$Sr$_2$CaCu$_2$O$_{8+\delta}$. *Science* **303**, 1995–1998 (2004).
14. Shen, K. M. *et al.* Nodal quasiparticles and antinodal charge ordering in Ca$_{2-x}$Na$_x$CuO$_2$Cl$_2$. *Science* **307**, 901–904 (2005).
15. Fauqué, B. *et al.* Magnetic order in the pseudogap phase of high-T_c superconductors. *Phys. Rev. Lett* **96**, 197001 (2006).
16. Kohsaka, Y. *et al.* An intrinsic bond-centered electronic glass with unidirectional domains in underdoped cuprates. *Science* **315**, 1380–1385 (2007).
17. Doiron-Leyraud, N. *et al.* Quantum oscillations and the fermi surface in an underdoped high-t_c superconductor. *Nature* **447**, 565–568 (2007).
18. Xia, J. *et al.* Polar kerr-effect measurements of the high-temperature YBa$_2$Cu$_3$O$_{6+x}$ superconductor: Evidence for broken symmetry near the pseudogap temperature. *Phys. Rev. Lett* **100**, 127002 (2008).
19. Li, Y. *et al.* Unusual magnetic order in the pseudogap region of the superconductor HgBa$_2$CuO$_{4+\delta}$. *Nature* **455**, 372–375 (2008).
20. Wise, W. D. *et al.* Charge-density-wave origin of cuprate checkerboard visualized by scanning tunnelling microscopy. *Nat. Phys* **4**, 696–699 (2008).
21. Hinkov, V. *et al.* Electronic liquid crystal state in the high-temperature superconductor YBa$_2$Cu$_3$O$_{6.45}$. *Science* **319**, 597–600 (2008).
22. Grilli, M., Seibold, G., Di Ciolo, A. & Lorenzana, J. Fermi surface dichotomy in systems with fluctuating order. *Phys. Rev. B* **79**, 125111 (2009).
23. Daou, R. *et al.* Broken rotational symmetry in the pseudogap phase of a high-T_c superconductor. *Nature* **463**, 519–522 (2010).
24. Lawler, M. J. *et al.* Intra-unit-cell electronic nematicity of the high-T_c copper-oxide pseudogap states. *Nature* **466**, 347–351 (2010).
25. Parker, C. V. *et al.* Fluctuating stripes at the onset of the pseudogap in the high-T_c superconductor Bi$_2$Sr$_2$CaCu$_2$O$_{8+x}$. *Nature* **468**, 677–680 (2010).
26. He, R.-H. *et al.* From a single-band metal to a high-temperature superconductor via two thermal phase transitions. *Science* **331**, 1579–1583 (2011).

27. Mesaros, A. *et al.* Topological defects coupling smectic modulations to intra–unit-cell nematicity in cuprates. *Science* **333,** 426–430 (2011).

28. Fujita, M., Goka, H., Yamada, K., Tranquada, J. M. & Regnault, L. P. Stripe order, depinning, and fluctuations in $La_{1.875}Ba_{0.125}CuO_4$ and $La_{1.875}Ba_{0.075}Sr_{0.050}CuO_4$. *Phys. Rev. B* **70,** 104517 (2004).

29. Abbamonte, P. *et al.* Spatially modulated 'mottness' in $La_{2-x}Ba_xCuO_4$. *Nat. Phys* **1,** 155–158 (2005).

30. Birgeneau, R. J., Stock, C., Tranquada, J. M. & Yamada, K. Magnetic neutron scattering in hole-doped cuprate superconductors. *J. Phys. Soc. Jpn* **75,** 111003 (2006).

31. Wu, H.H. *et al.* Charge stripe order near the surface of 12-percent doped $La_{2-x}Sr_xCuO_4$. *Nat. Commun.* **1023,** 1–5 (2012).

32. LeBoeuf, D. *et al.* Electron pockets in the fermi surface of hole-doped high-t_c superconductors. *Nature* **450,** 533–536 (2007).

33. Laliberté, F. *et al.* Fermi-surface reconstruction by stripe order in cuprate superconductors. *Nat. Commun.* **2,** 432 (2011).

34. Wu, T. *et al.* Magnetic-field-induced charge-stripe order in the high-temperature superconductor $YBa_2Cu_3O_y$. *Nature* **477,** 191–194 (2011).

35. Ghiringhelli, G. *et al.* Long-range incommensurate charge fluctuations in $(Y,Nd)Ba_2Cu_3O_{6+x}$. *Science* **337,** 821–825 (2012).

36. Chang, J. *et al.* Direct observation of competition between superconductivity and charge density wave order in $YBa_2Cu_3O_{6.67}$. *Nat. Phys.* **8,** 871–876 (2012).

37. Achkar, A. J. *et al.* Distinct charge orders in the planes and chains of ortho-III-ordered $YBa_2Cu_3O_{6+\delta}$ superconductors identified by resonant elastic X-ray scattering. *Phys. Rev. Lett* **109,** 167001 (2012).

38. Hossain, M. A. *et al. In situ* doping control of the surface of high-temperature superconductors. *Nat. Phys.* **4,** 527–531 (2008).

39. Damascelli, A., Hussain, Z. & Shen, Z.-X. Angle-resolved photoemission studies of the cuprate superconductors. *Rev. Mod. Phys.* **75,** 473–541 (2003).

40. Fischer, O., Kugler, M., Maggio-Aprile, I., Berthod, C. & Renner, C. Scanning tunneling spectroscopy of high-temperature superconductors. *Rev. Mod. Phys.* **79,** 353–419 (2007).

41. Hanaguri, T. *et al.* A 'checkerboard' electronic crystal state in lightly hole-doped $Ca_{2-x}Na_xCuO_2Cl_2$. *Nature* **430,** 1001–1005 (2004).

42. Zhiqiang, M. *et al.* Multiple $Bi_2Sr_{2-x}Ba_xCuO_y$ microstructures and the effect of element doping (Ba,La,Pb) on the 2:2:0:1 phase. *Phys. Rev. B* **47,** 14467–14475 (1993).

43. Lee, T. J. *et al.* X-ray structure analysis of Bi2212 using synchrotron source and high dynamic range imaging plate detector. *Chin. J. Phys.* **38,** 243–261 (2000).

44. Mans, A. *et al.* Experimental proof of a structural origin for the shadow fermi surface of $Bi_2Sr_2CaCu_2O_{8+\delta}$. *Phys. Rev. Lett.* **96,** 107007 (2006).

45. King, P. D. C. *et al.* Structural origin of apparent fermi surface pockets in angle-resolved photoemission of $Bi_2Sr_{2-x}La_xCuO_{6+\delta}$. *Phys. Rev. Lett* **106,** 127005 (2011).

46. Aebi, P. *et al.* Complete fermi surface mapping of $Bi_2Sr_2CaCu_2O_{8+x}$ (001): coexistence of short range antiferromagnetic correlations and metallicity in the same phase. *Phys. Rev. Lett* **72,** 2757–2760 (1994).

47. Zhiqiang, M. *et al.* Relation of the superstructure modulation and extra-oxygen local-structural distortion in $Bi_{2.1-y}Pb_ySr_{1.9-x}La_xCuO_z$. *Phys. Rev. B* **55,** 9130–9135 (1997).

48. Wochner, P., Tranquada, J. M., Buttrey, D. J. & Sachan, V. Neutron-diffraction study of stripe order in $La_2NiO_{4+\delta}$ with $\delta = 2/15$. *Phys. Rev. B* **57,** 1066–1078 (1998).

49. Milward, G. C., Calderon, M. J. & Littlewood, P. B. Electronically soft phases in manganites. *Nature* **433,** 607–610 (2005).

Acknowledgements

Author contributions

Additional information

SUPPLEMENTARY FIGURES

Supplementary Figure S1: LEED doping and temperature dependence of Bi2201, for (a) UD23K ($p = 0.14$) and (b) OP30K ($p = 0.16$) samples. A period-8 $\mathbf{Q}_2 = \mathbf{Q}_1/2$ modulation is present in UD23K, but temperature-independent, while no $\mathbf{Q}_2$ modulation is observed in OP30K. (c) ARPES MDCs along the nodal cut $\Gamma - Y$ around the Fermi crossing of the main band, shown for UD23K, in the same configuration as for the UD15K ARPES data in the main text [Supplementary Figure 1(d)]; ARPES, in agreement with the LEED results, provide evidence for a $\mathbf{Q}_2$ surface modulation in UD23K that is temperature independent and fixed to the bulk value. (d) Similar MDCs for OP30K show no indication of $\mathbf{Q}_2$-derived bands.
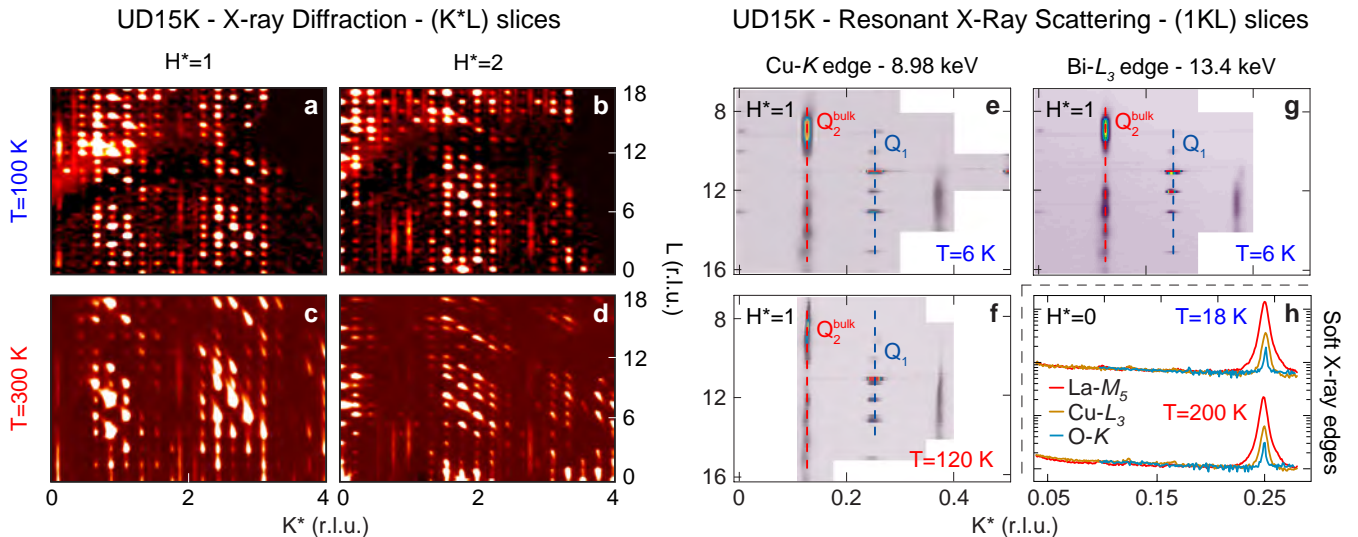
Supplementary Figure S2: X-ray results on UD15K Bi2201. Left panels: $\mathbf{K}^*$-$\mathbf{L}$ sections of the X-ray diffraction maps, taken at $T = 100$ K, $H^* = 1$ (a), and $H^* = 2$ (b) – and $T = 300$ K, $H^* = 1$ (c), and $H^* = 2$ (d). Right panels: resonant hard X-ray scattering $\mathbf{K}^*$-$\mathbf{L}$ maps ($H^* = 1$) with photon energy tuned to the Cu-K edge, $T = 6$ K (e) and $T = 120$ K (f) – and Bi-L_3 edge, $T = 6$ K (g). (h) Scattering scans along $\mathbf{K}^*$ for the soft X-ray edges: La-M_5 (red, $L = 2.05$), Cu-L_3 (yellow, $L = 2.05$) and O-K (blue, $L = 1.1$), acquired at 18 K (top) and 200 K (bottom). Note: in (h) the intensity is plotted on a logarithmic scale, and the 18 K profiles have been offset for clarity.
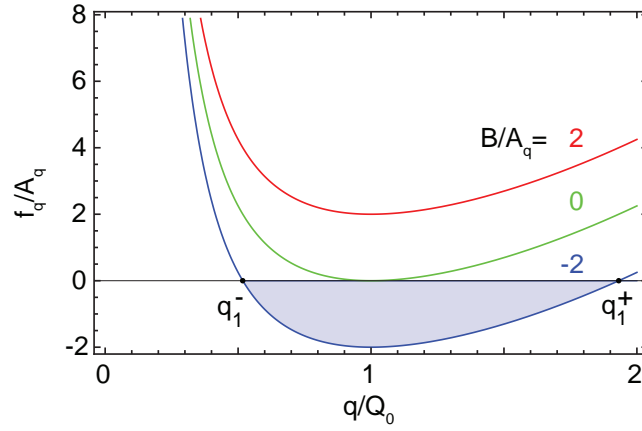
Supplementary Figure S3: f_q profiles for several values of $B/A_q = -2, 0, 2$ (blue, green, and red curves, respectively). The shaded region shows the range of wavevectors, $q_1^- \to q_1^+$ for the 1$^{\text{st}}$ harmonic, for which the system can lower its energy by having a nonzero CDW amplitude.
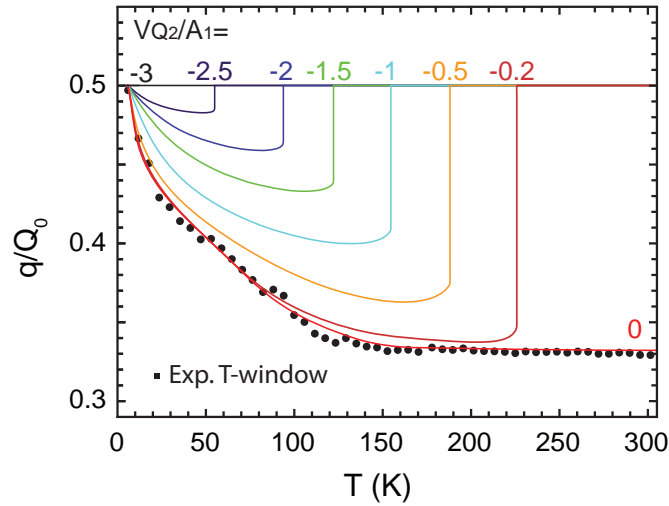
Supplementary Figure S4: The effect of the V_{Q_2} potential for the structural bulk Q_2 wavevector, showing suppression of the temperature-dependence of the CDW wavevector. Here $(V_{\text{L}}, V_{Q_1}) = (0, -.15)$, and the red, magenta, orange, cyan, green, blue, purple, and black curves correspond to $V_{Q_2}/A_1 = 0$, -0.2 , -0.5, -1, -1.5, -2, -2.5, and -3 respectively. Black dots represent experimental data from LEED. The jump in the wavevector for nonzero V_{Q_2} shows the pinning of the CDW to the bulk Q_2 structure near $Q_1/2$, with complete suppression of the temperature-dependence beyond $V_{Q_2}/A_1 = -3$.
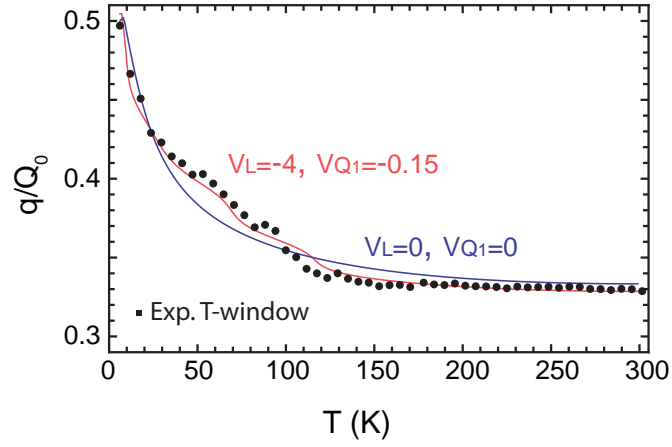
Supplementary Figure S5: CDW wavevector obtained by numerical minimization of the free-energy for the first and third harmonic only. The blue curve is for $(V_L, V_{Q_1}) = (0, 0)$, and the red curve has $(V_L, V_{Q_1}) = (-4, -.15)$. ($A_1 = 162$, $A_3 = 2.05 \times A_1$, $C = 200$, $Q_0 = 1$). Black dots are the LEED experimental data.
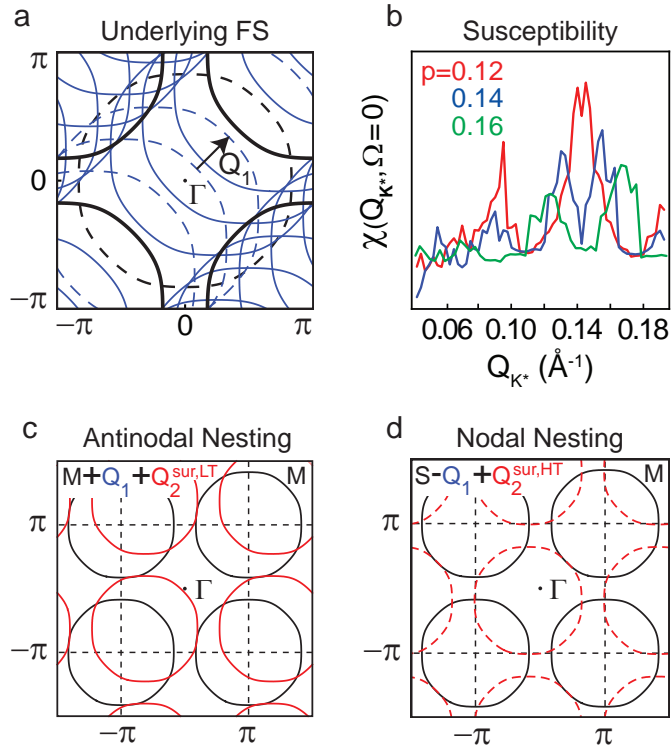
Supplementary Figure S6: Tight-binding fit of the experimental Fermi surface (a) for underdoped Bi2201, ($x = 0.8$, $p = 0.12$). The main band and its $\mathbf{Q}_1$ replicas are shown in black and blue, respectively, with folded ortho-derived features (shadow bands) dashed. Nesting-susceptibility calculated from the tight-binding Fermi surface (b) is shown for $p = 0.12$ (red), 0.14 (blue) and 0.16 (green). For $p = 0.12$, there are two peaks near $q = 0.095$ and $q = 0.14\,\text{Å}^{-1}$, corresponding to nodal and antinodal nesting, (c,d) respectively. The weaker nodal peak disappears with increased hole-doping, while the antinodal peak splits into two progressively smaller and broader peaks.
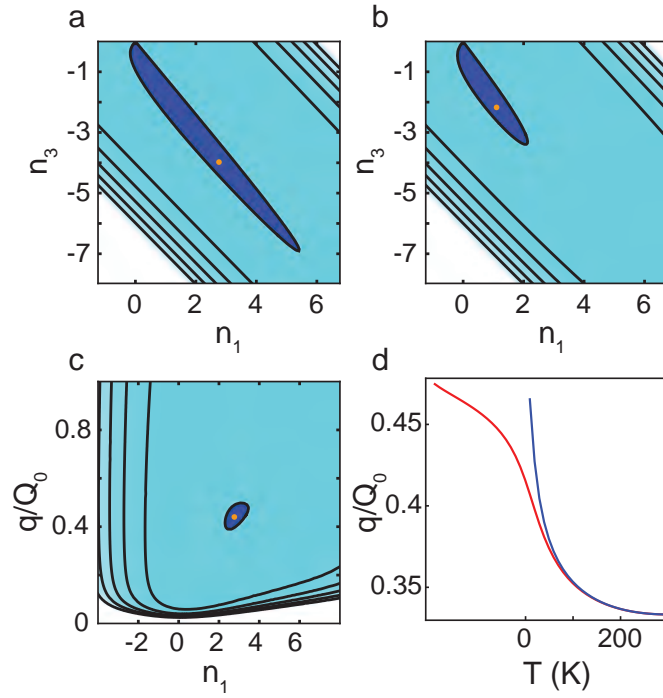
Supplementary Figure S7: Contour plots of the free-energy including just the first and third harmonics, evaluated at the q-value in (a-b), and n_3 in (c), corresponding to the global minimum in the free-energy (orange point), and $T = 15\,\mathrm{K}$. (a) shows the effect of the approximation in Eq. S7 on flattening the free-energy compared to (b). (d) shows the temperature-dependence of the wavevector of the global minimum corresponding to (a,blue) and (b,red).
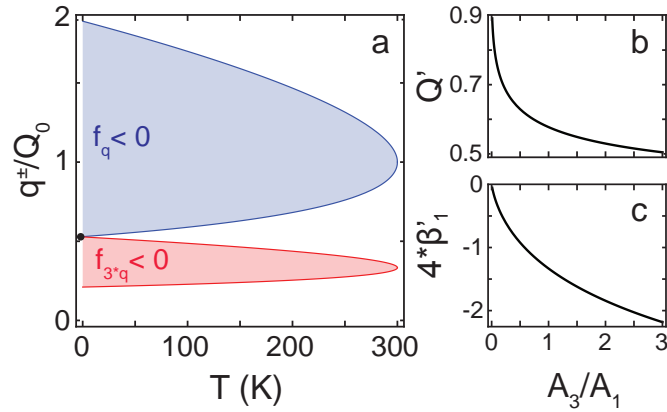
Supplementary Figure S8: (a) Curves showing the wavevector where the f_q potential crosses zero for the first and third harmonic ($A_3 = 2.05 \times A_1$), in blue and red respectively. The shaded regions in (a) show the range of wavevectors for which the respective potential is negative. The black dot is the temperature and wavevector at which both potentials become negative at (Q', T'). The value of A_1 is set by the relations shown in (b-c) for the experimental results in Supplementary Figure S5, to yield the temperature axis of the experiment.

SUPPLEMENTARY NOTES

Supplementary Note 1 | LEED/ARPES and X-ray doping and temperature dependence

LEED/ARPES doping and temperature dependence. The doping and temperature dependence of the $\mathbf{Q}_2$ superstructural modulations is shown in Supplementary Figure S1 for UD23K and OP30K samples. The appearance of the $\mathbf{Q}_2$ modulation in UD23K and UD15K samples is in contrast to OP30K, where only the $\mathbf{Q}_1$ modulation is observed in both LEED and ARPES. In addition, the observation of the $\mathbf{Q}_2$ modulation in UD23K is also at variance with the temperature dependence discussed in the main text for UD15K, as the LEED and ARPES diffraction features associated with the $\mathbf{Q}_2$ wavevector remain temperature-independent in UD23K at the value of the bulk/low-T surface $\mathbf{Q}_2$ in UD15K.

Temperature-dependent X-ray scattering. X-ray diffraction (XRD) and resonant scattering (REXS) data on UD15K as a function of temperature are displayed in Supplementary Figure S2. XRD maps show no qualitative difference between low- [$T = 100$ K, Supplementary Figure S2(a,b)] and high-temperature [$T = 300$ K, Supplementary Figure S2(c,d)]. Although the different acquisition parameters yield a slightly different contrast and signal-to-noise ratio in the intensities, the rod-like period-8 features exhibit the same pattern, showing no evolution from 300 to 100 K. REXS data at the Cu-K edge (8.98 keV) show no signs of temperature dependence, as well [see Supplementary Figure S2(e,f)]. The scattering map acquired on the Bi-L_3 edge (13.4 keV), plotted in Supplementary Figure S2(g), is qualitatively indistinguishable from the Cu-K edge, a signature that the associated period-8 modulation is ubiquitous in the unit cell. The $\mathbf{Q}_2^{\text{bulk}}$ rods are absent in the soft X-ray scattering scans [Supplementary Figure S2(h)], consistently with the XRD results for the basal plane $H^* = 0$ [see Fig. 3(a) in the main text], whereas the $\mathbf{Q}_1$-related peak (at $H^* \sim 0.25$) exhibit a clear enhancement at all the investigated absorption edges, thus reflecting the presence of a well-defined near-period-4 modulation throughout the entire unit cell.

Supplementary Note 2 | Ginzburg-Landau description of a charge-density wave.

Ginzburg-Landau theory. Mean-field theory has been well utilized since the work of Landau, and has since been expanded and applied to describe many thermal and statistical systems, which typically possess phase transitions and ordering behavior. In particular, Ginzburg-Landau mean-field theory is used to explain the onset of a charge-density-wave (CDW) below a critical temperature, with a wavevector and amplitude given by the microscopic details of the problem [50-53]. Recently, Ginzburg-Landau theory was shown to be effective at describing a soft electronic phase [49], in which an additional interplay with magnetic order leads to charge-ordering with doping- and temperature-dependent wavelength.

To relate to the temperature-dependence of $\mathbf{Q}_2$ in our measurements of underdoped Bi2201, we have constructed a similar mean-field free-energy functional $F[\psi]$ [49-53] and solved this model based on numerical minimization of F with respect to its order parameter ψ. The main result of this study is to connect the $\mathbf{Q}_2$ temperature-dependence observed with LEED to the temperature-dependent harmonic content of the CDW. In addition, the calculation of the Fermi surface nesting susceptibility function provides information regarding the low and high-temperature endpoints of the observed temperature-dependence. Note that, in relation to T^* and the pseudogap in the underdoped cuprates, our model does not incorporate any additional order parameter besides the CDW and a static $\mathbf{Q}_1$ modulation.

Mean-field free-energy. The order parameter of the model is the charge-density, which is Fourier transformed according to the following equation:

$$n(x) = \sum_q n_q e^{iqx} \,. \tag{S1}$$

This way the problem can be reformulated in momentum space. Only the even-order terms in $F[\psi]$ are considered

(due to symmetry between positive and negative CDW amplitude as described in Ref. 52), of the form:

$$F_2 = \sum_q f_q |n_q|^2$$

$$f_q = A_q \left(\frac{q}{Q_0} - \frac{Q_0}{q}\right)^2 + B \tag{S2}$$

$$F_4 = C \int n(x)^4 dx.$$

The second-order F_2 term is a summation of f_q, which contains a combination of a gradient-term ($\propto q^2$) preventing short wavelength oscillations, and a Coulomb term which screens long wavelength oscillations ($\propto 1/q^2$), so that f_q is minimized by $q = Q_0$, a temperature-independent wavevector set by the microscopic details. The factors A_q and C are also temperature-independent and positive, and B is linearly dependent on temperature and changes sign at the CDW critical temperature : $B \to \tilde{B}(T - T_{\text{CDW}})$ [53]. Supplementary Figure S3 shows the shape of the f_q potential, which implies that for $T < T_{\text{CDW}}$ the system can lower its free-energy by having nonzero CDW amplitude for wavevectors in the range corresponding to the shaded region (i.e. when f_q is negative, which requires that $B/A_q < 0$).

Recall that the summation over wavevectors in F_2 is due to the Fourier-transform of the charge-density in Eq. S1. However, if the charge-density is a periodic function ($q = 2\pi/\lambda$), it can be represented as a Fourier-series:

$$n(x) = \sum_{j=-\infty}^{\infty} n_j \, e^{i\,(jq\cdot x)}, \tag{S3}$$

which naturally leads to the notion of harmonics, which have shorter wavelengths corresponding to integer multiples of the wavevector, $j * q$. This allows us to mathematically treat a single, general waveform for the charge-density as a superposition of these harmonics. The free-energy F_2 in Eq. S2 therefore involves the summation of f_q evaluated for the harmonics. This gives terms in the free-energy $\propto f_{j*q}$, which are minimized by wavevector q_0 satisfying $j * q_0 = Q_0$. Thus the f_{j*q} term is negative for wavevectors between the two values $q_j^{\pm}$ given by:

$$\frac{q_j^{\pm}}{Q_0} = \frac{1}{j}\sqrt{1 - 2\beta \pm 2\sqrt{\beta^2 - \beta}} \; ; \; \beta \equiv B/4A_q. \tag{S4}$$

In the quadratic term F_2, the wavevectors $q_j^- \to q_j^+$ (for j^{th} harmonic) set the range for energetically favorable CDW amplitude, as a function of the temperature ($T \propto \beta$ in Eq. S4).

The fourth order term F_4 prevents divergence of the amplitude of $n(x)$. Together with the lack of a third-order term in the free-energy [52], this leads to a situation where only odd harmonics of the charge-density-wave occur in the wavevector expansion of the free-energy; for the other terms, the phase factors of the momentum representation of $n(x)^4$ terms do not cancel, and the integral in Eq. S2 is oscillatory and averages to zero. These considerations allow us to rewrite Eq. S1 as:

$$n(x) \to \sum_m n_m e^{imqx} \; ; \; m = \pm 1, \pm 3, \pm 5, ... \tag{S5}$$

Furthermore, since we expect the charge-density $n(x)$ to be a real function, this gives the requirement that $n_q = n_{-q}$. When we compute F_4 in momentum-space, we obtain the following integral:

$$C \int dx \sum_{m_1...m_4} n_{m_1} n_{m_2} \, n_{m_3} \, n_{m_4} \, e^{iqx(m_1+m_2+m_3+m_4)}. \tag{S6}$$

This results in the condition that $m_1 + m_2 + m_3 + m_4 = 0$, however since $n_q = n_{-q}$, we are free to switch the sign of any m_i, so that we may instead write $m_1 + m_2 + m_3 - m_4 = 0$, and all other combinations of signs, which can be satisfied for certain combinations of positive and odd indexes m_i. This yields:

$$F_4 \to C \sum_{m_1...m_4} n_{m_1} \, n_{m_2} \, n_{m_3} \, n_{m_4} \cong C \left(\sum_i n_i\right)^4, \tag{S7}$$

(i odd and positive)

leading to the free-energy functional that is sufficient to describe the experimental wavevector on underdoped Bi2201, by *identifying the wavevector* $Q_0 \rightarrow Q_1$:

$$
\begin{aligned}
F = &\left(A_1 (\frac{q}{Q_1} - \frac{Q_1}{q})^2 + B \right) |n_1|^2 \\
&+ \left(A_3 (\frac{3q}{Q_1} - \frac{Q_1}{3q})^2 + B \right) |n_3|^2 \\
&+ C(n_1 + n_3)^4 \,.
\end{aligned}
\tag{S8}
$$

Note that the right-hand side in Eq. S7 is written as approximate because it includes cross-terms which do not satisfy the constraint that the subindex sum is zero, and which will cancel in the integral Eq. S6. Here we consider only the first and third harmonics, then we just have one extra term of this kind, $4Cn_3^3 n_1$. In Eq. S8 we keep the full term corresponding to the approximation in Eq. S7. This is due to the short correlation lengths observed for the temperature-dependent wavevector in ARPES and LEED, which are connected to finite-size effects resulting in a flattening of the free-energy near the minimum (see Ginzburg-Landau model appendix).

To compare with the experimental finding of commensurability effects in the LEED wavevector temperature-dependence, the model of Eq. S8 is supplemented by potentials which can account for the attractive forces experienced when the lattice is commensurate with the CDW (integer multiple of the wavelength), as well as the repulsive forces for intermediate wavelengths (incommensurate, non-integer). Commensurability with the bulk $\mathbf{Q}_2$ modulation, as found by X-ray diffraction, arises naturally by considering an additional periodic potential:

$$
\begin{aligned}
F_{Q_2} &= \int V(x)\, n(x)\, dx \\
&= \int V_{Q_2}\, e^{iQ_2 x}\, n(x)\, dx \simeq \frac{V_{Q_2}\, n_1}{\epsilon + |q - Q_2^{\text{bulk}}|} \,.
\end{aligned}
\tag{S9}
$$

Where the additional ϵ term is needed to turn the singularity at $q = Q_2^{\text{bulk}}$ into a finite peak, for numerical convergence, and only includes the first harmonic, n_1, as there is no need to consider higher harmonics matching Q_2^{bulk}, which would lead to a first harmonic with unecessarily long wavelength ($q << Q_2^{\text{bulk}}$). For negative V_{Q_2} the system is attracted to the Q_2^{bulk} wavevector, which is favored when V_{Q_2} is larger in magnitude than the energy cost from the other terms in the free-energy. The effect of the Q_2^{bulk} potential, V_{Q_2}, is shown in Supplementary Figure S4, for various strengths of the potential. This potential causes the CDW to lock in to the bulk structural modulation wavevector ($q = Q_2^{\text{bulk}}$), and acts to suppress the temperature-dependence. The limiting cases $V_{Q_2} = 0$ and $V_{Q_2} >> 0$ represent the surface (LEED/ARPES) and bulk (REXS/XRD) temperature-dependence, respectively. Intermediate values of V_{Q_2} describe the region just below the surface, which shows a CDW with reduced dependence on temperature, and instability towards first-order lock-in transitions to the $q = Q_2^{\text{bulk}}$ wavevector. An additional potential can be added to account for the tendency of the CDW to be commensurate with the orthorhombic lattice [53]:

$$
F_{\text{L}} = V_{\text{L}} \left(n_1^2 + n_3^2 + \cdots \right) \cos(\frac{2\pi G}{q}) \,,
\tag{S10}
$$

where G is a reciprocal lattice vector, such that with the inclusion of F_{L} in the free-energy, the system is weakly attracted to wavevectors for which $q = G/j$, for integer j, provided that V_{L} is negative. These wavevectors correspond to a CDW wavelength that is an integer multiple of the lattice constant, $\lambda_{\text{CDW}} = j \times b^*$. A similar potential can be included for the static Q_1 modulation observed in Bi2201, which is identical except for the replacement $G \rightarrow Q_1$; this leads to the expression:

$$
F_{Q_1} = V_{Q_1} \left(n_1^2 + n_3^2 + \cdots \right) \cos(\frac{2\pi Q_1}{q}) \,.
\tag{S11}
$$

Recall that the wavevector from the experiment shows commensurability with both the lattice and Q_1. The endpoints of the temperature-dependence occur at $q = Q_1/2$ and $q = Q_1/3$, and this commensurability to Q_1 is already present in the free-energy of Eq. S8. However, the additional commensurability potential in Eq. S11 accounts for a weak repulsion on intermediate wavevectors (incommensurate with Q_1).

Ginzburg-Landau theory results. Supplementary Figure S5 shows the CDW wavevector obtained by numerical minimization of the free-energy for the first and third harmonic only, in the temperature region $0 < T < T_{\text{CDW}}$. The

parameter values $A_1 = 162$ and $A_3 = 2.05 \times A_1$ were chosen to have $T_{\text{CDW}} \geq 300\,\text{K}$, following the fact that we observe Q_2 with LEED up to room temperature, and to scale the temperature of the model to that of the ARPES/LEED experiments (see Ginzburg-Landau model appendix). The potential V_B is zero to model the surface of the crystal, and the results for both $(V_{\text{L}}, V_{\text{Q}_1}) = (0, 0)$ and $(V_{\text{L}}, V_{\text{Q}_1}) = (-4, -.15)$ are shown in Supplementary Figure S5. The V_{Q_1} potential has a moderate flattening effect on the shape of the temperature-dependence of the CDW wavevector between $Q_1/2$ and $Q_1/3$, and improves the agreement with the experiment. Additional inclusion of the lattice commensurability potential, V_{L}, creates inflection points in agreement with the LEED temperature-dependence. These inflection points are larger than the experimental temperature window of the LEED data acquisition, and are in qualitative agreement with the effect of the lattice commensurability free-energy potential, V_{L}. The existing quantitative discrepancies (in particular for $n = 9$) between the data and the Ginzburg-Landau model might be related to error in the determination of the sample temperature and the LEED wavevector in the experiment. Nevertheless, this suggests significance in the qualitative appearance of features indicating a tendency towards commensurability with the orthorhombic reciprocal lattice vector, and additionally the periodic lattice distortion, Q_1.

Ginzburg-Landau model appendix. As mentioned in the text, the approximation in Eq. S7 involves an additional term in the free-energy, $4Cn_3^3 n_1$, which is forbidden by the integration in Eq. S6. Re-including only the lowest order term that is excluded, can be understood to originate from finite-size effects connected to the short coherence-lengths seen in ARPES and LEED for the surface. The LEED spots have a half-width at half-maximum corresponding to a coherence-length of ~ 15Å, so that the electronic coherence-length is smaller than the Q_2 wavelength (~ 45Å at low-temperature). The short LEED coherence-length could be caused by the formation of domains with random local deviation in the Q_2 value, for instance due to impurities. The finite domain variations in the integral (S6) will reintroduce these forbidden terms, in particular the lowest order ones, that contain the longest wavelength ocillation in the integrand of Eq. S6. This suggests that an impurity driven "finite-size" interaction between the CDW harmonics can play a role in the soft-wavevector phase. This is also consitent with the bulk/surface dichotomy that is observed, as the coherence lengths for Q_2 from bulk X-ray measurements are an order of magnitude larger (~ 500Å) than those seen with surface-sensitive probes (~ 50Å).

Supplementary Figure S7(a-c) shows that a well-shaped minimum of the free-energy occurs at a particular wavevector, q, and charge-density amplitudes, n_1 and n_3. In Supplementary Figure S7(a-b,d) the effect of the approximation in Eq. S7 is shown to cause a flattening of the free-energy along the line $n_1 = -n_3$. Supplementary Figure S7(d) shows the sharp temperature-dependence that develops due to this flattening of the free-energy. This results in a low-temperature instability, illustrated in Supplementary Figure S8(a), which highlights the range of temperatures and wavevectors for which the f_q potentials are negative. There is a tendency to increase either n_1 or n_3, in the corresponding shaded region for each wavevector, in order to lower the energy of the system. In the range of temperatures for which the two potentials cannot be simultaneously negative for any wavevector, the system will have a temperature dependent CDW wavevector resulting from the balance of the n_1 and n_3 terms. The amplitudes of these terms will be opposite in sign in order to minimize the $F_4 = C(n_1 + n_3)^4$ energy cost, while trying to increase (decrease) the component which has a negative (positive) potential at a given wavevector. Just below T_{CDW} the system can reduce its energy by having $q = Q_0$ ($Q_0/3$) in the case of $A_1 > A_3$ ($A_3 > A_1$).

There is a region in Supplementary Figure S8(a), where both f_q potentials are negative, below a temperature $T' = 4A_1\beta_1'$. In this region both n_1 and n_3 will increase to lower the free-energy, but they are also free to take opposite sign in order to cancel the fourth order term energy cost. For any wavevector in the overlap region, the free-energy can go arbitrarily negative by continuing to increase the charge-density while maintaining equal but opposite values for the first and third harmonic, leading to divergent behavior. Including higher order harmonics does not remedy the situation as long as the system is free to set these components to zero in the event they have a positive f_q value in this region. This creates an unphysical divergence in the CDW amplitude for $q = Q'$ below T', which also results in a low-temperature instability that attracts the CDW wavevector to Q' even above T'.

Thus the experimental temperature range is scaled to the physical range $T' < T < T_{\text{CDW}}$. This can be done with $T' = A_1 * 4\beta_1' + T_{\text{CDW}}$, for β_1' given in Supplementary Figure S8(c). To explain the high-temperature behavior, $A_3 > A_1$ gives $q = Q_0/3$ just below T_{CDW}, and the low-temperature behavior is obtained by choosing A_3/A_1 to set Q', and choosing A_1 such that $T' < 0$ and thus outside the physical range considered. $T_{\text{CDW}} = 300\,\text{K}$ is chosen to represent the experimental observation of LEED diffraction peaks up to room temperature, though making this temperature higher does not have any significant impact on the temperature-dependence, and only gives a temperature-independent wavevector that persists at higher-temperatures. This effectively defines the temperature coefficient:

$$\tilde{B} = \frac{4A_1\beta_1'(A_3/A_1)}{300} \, . \tag{S12}$$

Such choice provides excellent agreement with experimental data for the parameters indicated in Supplementary Figure S5, which suggests that an impurity-driven enhancement of the CDW harmonic interaction could effectively indicate a flat or competing free-energy landscape playing a role in the surface CDW wavevector temperature-dependence.

Supplementary Note 3 | Fermi surface Nesting.

In addition the electronic susceptibility, or Lindhard function,

$$\chi_0 = \sum_k \frac{n_{\mathrm{F}}(\epsilon_{k+q}) - n_{\mathrm{F}}(\epsilon_k)}{\epsilon_k - \epsilon_{k+q}}, \tag{S13}$$

has been calculated for $p=0.12$ to $p=0.16$, from the tight-binding fit of the Fermi surface with hopping parameters extracted from the experimental ARPES Fermi surface [54] to accurately reproduce nesting for this material. The tight-binding model used for the calculation is depicted in Supplementary Figure S6(a) for $p = 0.12$, and includes the main band and shadow band, plus their $\mathbf{Q}_1$ replicas. The calculation is performed as described in Ref. 55, and the result is shown in Supplementary Figure S6(b). Two important nesting susceptibility peaks occur at $q = 0.140$ and $q = 0.095\,\text{Å}^{-1}$, which closely match the low and high-temperature values of the $\mathbf{Q}_2$-wavevector measured in the experiment. The effect of doping was incorporated by a shift of the chemical potential in the tight-binding model, thus changing the size of the Fermi surface, and resulting in the suppression of the $\mathbf{Q}_1/3$-peak and a gradual splitting, weakening and broadening of the $\mathbf{Q}_1/2$-peak [Supplementary Figure S6(b)]. This suggests that the $\mathbf{Q}_1/3$ instability only exists in a narrow range of dopings, and the $\mathbf{Q}_1/2$ peak in a comparatively larger range of dopings, near $p=1/8$. In particular, the $\mathbf{Q}_1/2$-peak comes from antinodal nesting between the main band (M) and its own $\mathbf{Q}_1$ replica [M+$\mathbf{Q}_1$, see also Supplementary Figure S6(c)], while the $\mathbf{Q}_1/3$-peak arises from nodal nesting between the main band (M) and the $\mathbf{Q}_1$ replica of the shadow band (S − $\mathbf{Q}_1$), as shown in Supplementary Figure S6(d).

For the antinodal nesting related to the $\mathbf{Q}_1/2$-peak, the reduced coherence at the antinode (due to the opening of the pseudogap) does not substantially affect the Lindhard function, for two reasons: (i) the main contribution to the antinodal peak in $\chi(Q_{\mathrm{K}^*})$ comes from the flat topology of the Fermi surface at the antinode (making the nesting quasi-1D); (ii) the largest antinodal nesting overlap [see Supplementary Figure S6(c)] occurs at a portion of the Fermi surface around $\phi = 10°$, where spectral weight is still substantially coherent [here ϕ represents the polar angle in k-space, measured from $\mathbf{k}=(\pi, \pi)$, with $\phi=0°$ corresponding to the antinode, $\phi=45°$ to the node]. This $\phi=10°$ value lies in the proximity of the gapless portion of the Fermi surface, the so-called "Fermi arcs", whose tips are located around $\phi=15 - 20°$.

SUPPLEMENTARY DISCUSSION

There are several important features of the mean-field model described here, in relation to the nontrivial temperature-dependence of the CDW wavevector, which arise due to interaction between the two lowest harmonics. The interplay of the CDW harmonics is connected with the influence of the structural $\mathbf{Q}_1$ modulation on the third CDW harmonic, $3\times\mathbf{Q}_2^{\mathrm{surf,HT}} = \mathbf{Q}_1$ at higher temperatures. Flattening the free-energy near the stable minimum results in enhanced interaction between harmonics of the surface CDW state, which is marked by a large temperature-dependence of the CDW wavevector, whose slope increases at low-temperatures. The reduction in the 3rd harmonic content at low-temperatures leads to a dramatic steepening of the charge-driven temperature-dependence of $\mathbf{Q}_2^{\mathrm{surf,LT}}$ at low-temperature, when it is near $\mathbf{Q}_2^{\mathrm{bulk}} = \mathbf{Q}_1/2$. This suggests that the surface experiences finite-size effects that result in a flattening of the energy-landscape, indicating electronic phase competition (see Ginzburg-Landau model appendix for details). Comparison to the measured wavevector from ARPES and LEED experiments gives remarkable agreement, which is improved after including a tendency towards commensurability with the lattice parameter b^* and the static structure modulation $\mathbf{Q}_1$.

Incorporating the effect of a periodic bulk potential, with wavevector $\mathbf{Q}_2^{\mathrm{bulk}} = \mathbf{Q}_1/2$ as determined by X-ray diffraction in underdoped Bi2201, results in suppression of the temperature-dependence. This suppression is related to the $\mathbf{Q}_2^{\mathrm{bulk}}$ modulation, which pins the CDW wavevector to the structural modulation in the underlying bulk, resulting in temperature-dependence of the CDW wavevector occuring only near the surface, and thus leading to a static bulk structure and charge-density wave, while the surface can evolve energetically. A nesting-driven, electronic response peak at the Fermi energy is apparently connected to the bulk supermodulation and the surface CDW at low-temperature ($\mathbf{Q}_2^{\mathrm{bulk}} = \mathbf{Q}_2^{\mathrm{surf,LT}} = \mathbf{Q}_1/2$), and at high-temperature ($\mathbf{Q}_2^{\mathrm{surf,HT}} = \mathbf{Q}_1/3$). As a final remark, we note that the apparently weaker $\mathbf{Q}_1/3$ peak in the (nodal) nesting susceptibility does not necessarily correlate to the strength of the instability, as has been noted in the chalcogenide CDW superconductors [56].

SUPPLEMENTARY REFERENCES

50. McMillan, W. L. Landau theory of charge-density waves in transition-metal dichalcogenides. *Phys. Rev. B* 12, 1187 (1975).

51. Toledano, J. C. & Toledano, P. The Landau Theory of Phase Transitions. 1987, World Scientific.

52. Turgut, S. & Falicov, L. M. Phenomenological Ginzburg-Landau theory of charge-density-wave spectra. *Phys. Rev. B* **50**, 8221 (1994).

53. Grüner, G. Density Waves In Solids. Frontiers in Physics 1994, Perseus.

54. King, P. D. C. *et al.* Structural Origin of Apparent Fermi Surface Pockets in Angle-Resolved Photoemission of $Bi_2Sr_{2-x}La_xCuO_{6+\delta}$. *Phys. Rev. Lett.* **106**, 127005 (2011).

55. Inosov, D.S. *et al.* Fermi surface nesting in several transition metal dichalcogenides. *New J. Phys.* **10**, (2008).

56. Johannes, M. D. & Mazin, I. I. Fermi surface nesting and the origin of charge density waves in metals. *Phys. Rev. B* **77**, 165135 (2008).